

Unsteady Flow Separation and High Performance of Airfoil with Local Flexible Structure at Low Reynolds Number

Peng-Fei Lei¹, Jia-Zhong Zhang^{1,*}, Wei Kang², Sheng Ren¹ and Le Wang¹

¹ School of Energy and Power Engineering, Xi'an Jiaotong University, Xi'an 710049, P.R. China.

² School of Astronautics, Northwestern Polytechnical University, Xi'an 710072, P.R. China.

Received 11 October 2013; Accepted (in revised version) 9 May 2014

Communicated by Rho Shin Myong

Available online 24 June 2014

Abstract. The unsteady flow separation of airfoil with a local flexible structure (LFS) is studied numerically in Lagrangian frames in detail, in order to investigate the nature of its high aerodynamic performance. For such aeroelastic system, the characteristic-based split (CBS) scheme combined with arbitrary Lagrangian-Eulerian (ALE) framework is developed firstly for the numerical analysis of unsteady flow, and Galerkin method is used to approach the flexible structure. The local flexible skin of airfoil, which can lead to self-induced oscillations, is considered as unsteady perturbation to the flow. Then, the ensuing high aerodynamic performances and complex unsteady flow separation at low Reynolds number are studied by Lagrangian coherent structures (LCSs). The results show that the LFS has a significant influence on the unsteady flow separation, which is the key point for the lift enhancement. Specifically, the oscillations of the LFS can induce the generations of moving separation and vortex, which can enhance the kinetic energy transport from main flow to the boundary layer. The results could give a deep understand of the dynamics in unsteady flow separation and flow control for the flow over airfoil.

AMS subject classifications: 74F10, 76G25, 76D55, 76D05

Key words: Unsteady flow, moving separation, aeroelastic structure, lift enhancement, Lagrangian coherent structures.

*Corresponding author. *Email addresses:* pfllei@stu.xjtu.edu.cn (P.-F. Lei), jzzhang@mail.xjtu.edu.cn (J.-Z. Zhang), wkang@nwpu.edu.cn (W. Kang), rensheng901728@126.com (S. Ren), wangled@163.com (L. Wang)

1 Introduction

Flexible structures, such as shell, plate, shallow arch and membrane etc., have been used widely in the high-performance aircraft, especially in micro air vehicles [1–3]. Many experiments and numerical researches have shown that the flexible airfoil, compared with the rigid one, can delay flow separation, enhance lift and reduce drag efficiently [2, 4–8]. At low Reynolds number, flow separation can easily occur for laminar flow, and result in complex unsteady separated flow, even the transition to turbulence. In such flow, small perturbation, such as the oscillation of flexible structure, can change the flow structure and airfoil performance dramatically. Chimakurthi et al. [6] presented a computational aeroelasticity framework for the flapping wing micro air vehicles, and investigated both rigid and flexible wing. Lee et al. [7] studied the two-dimension insect flapping wing, and found that structural flexibility has a significant impact on aerodynamic performance. Also, some key physical phenomena, such as vortex pairing and vortex staying, were observed. Kang et al. [8] introduced the local flexible structure to control the flow, and improved the aerodynamical performance significantly. Compared with the fully flexible wing, local flexible structure is easier to implement active control, and can be used in normal or large size airfoil. However, airfoil with flexible structure usually involves strong and complicated fluid-structure interaction, giving rise to a variety of phenomena relevant to the high aerodynamic performance. The unsteady flow separation, however, is generally the original source of many complex flow structures, such as vortex formation, wake flow etc. Therefore, a deep understanding of the unsteady flow separation and related flow structure can lead to a way to explain many complicated phenomena in unsteady flow.

Usually, the Eulerian descriptions of the flow are used to study the flow separation and flow structure, such as the streamline pattern, pressure and vorticity fields. However, there are many Lagrangian phenomena in the unsteady flow, such as flow separation, transient flow processes. These unsteady flow phenomena can be well described by the Eulerian description, yet their dynamic properties (e.g. fluid transport and mixing) are still hidden under Eulerian description. The Prandtl's criteria for flow separation, which are Eulerian description, indicate that the separation point is the point of vanishing wall-shear. However, in unsteady flow, vanishing wall shear does not denote separation in any meaningful sense [9]. As the development of nonlinear dynamics, Lagrangian description for flow has been increasingly appreciated by many researchers. Van Dammen [10] first studied boundary layer separation in Lagrangian frame, and gave the flow separation criteria from Lagrangian viewpoint. Duan and Wiggins [11] applied the lobe dynamics into the flow over circular cylinder to study the transport and mixing of vortex shedding in the near wake of circular cylinder in the point of dynamic view, and some new results have been found. Recently, it is shown that Lagrangian Coherent Structures (LCSs) proposed by Haller [12] become a useful tool to study flow structures in general unsteady flow from Lagrangian viewpoint. The LCSs are the transport barriers in unsteady flow, and hence it is convenient in the studies of transport in general unsteady

flow and transient flow by LCSs. More, the LCSs have been successfully used to study the flow separation [13, 14], vortex [15], oceanic flow [16], atmospheric flow [17] and turbulence [18, 19], etc.

In this paper, the self-induced oscillation of a local flexible structure (LFS) on the surface of airfoil is considered as a kind of small perturbation, to study its influence on the unsteady flow structure and aerodynamic performances of the airfoil. By the LCSs, the flow structures are analyzed in Lagrangian viewpoint, in order to understand the nature of unsteady flow separation, which is the key point of high aerodynamic performances of airfoil.

2 Unsteady flow separation and Lagrangian coherent structures

In this section, the unsteady separation, Lagrangian coherent structures and their relationship are introduced briefly. In a sense, the flow around a body can be considered as a dynamic system and described by the following equations,

$$\dot{x} = u(x, y, t), \quad \dot{y} = v(x, y, t), \quad (2.1)$$

where x and y are the Cartesian coordinates, u and v are velocity components.

For the steady flow, Eq. (2.1) is autonomous system, thus it's easy to apply the singular point theory to the stability analysis of the singular or fixed points and their stable and unstable manifolds in the flow field, which also can be seen from the streamline pattern directly, and these manifolds are the transport barriers in the flow pattern. However, the dynamic behaviors of the unsteady flow are complicated, and the streamlines cannot be considered as transport barriers. More, unsteady flow separation is much more complex than steady flow separation, and it is still an open problem in fluid dynamics.

It has been well-known that material spike is a common feature in both steady and unsteady flow separation [10, 13, 20] (see Fig. 1 in Ref. [13] for details of the formation of the material spike). In steady flow, the material spike coincides with the separation streamline. For unsteady flow, according to Haller [13], there are fixed separation and moving separation. Fixed separation is defined as a material instability induced by an unstable manifold of a distinguished boundary point, as shown in Fig. 1. In incompressible periodic flow, the fixed separation point $(\gamma, 0)$ should satisfy

$$\int_0^T u_y(\gamma, 0, t) dt = 0, \quad \int_0^T u_{xy}(\gamma, 0, t) dt < 0, \quad (2.2)$$

where x -axis coincides with the wall with no-slip boundary condition, (u, v) is the velocity field, T is the period of the flow. The unstable manifold of fixed separation point, coincides with the material spike, moves periodically in the flow and is invariant on the Poincaré section associated with the period of the flow.

Moving separation is a kind of separation that the material spike moves along the boundary, instead of stays near a fixed point as fixed separation. Therefore, moving material spike can move away from certain region near boundary, and should be considered

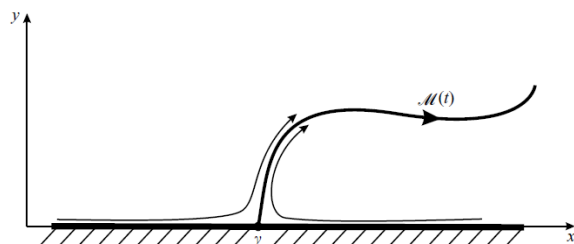


Figure 1: Schematics of fixed separation and its unstable manifold. [13]

as a finite-time phenomenon, which cannot be described by traditional unstable manifold.

In fact, the material spike is a attracting material line, and can be considered as a finite-time unstable manifold proposed by Haller [21]. The finite-time unstable manifold is stemmed from the property that the unstable manifold has maximum attracting rate, and defined as material lines which have local maximum repelling rate in finite time interval (t_0, t_0+T) . As time interval T increasing, the finite-time stable manifold can approach the invariant stable manifold exponentially. The finite-time stable manifolds, also called repelling LCSs, and finite-time unstable manifolds, also called attracting LCSs, form the LCSs in the flow [12]. Following the definitions, it is clear that the LCSs are the transport barriers in the flow, and the tangling of attracting and repelling LCSs indicates the transport and mixing of the flow. Above all, the LCSs can capture the material spikes in flow separation and vortex boundary, thus they are useful for the study of complex unsteady phenomena.

The numerical analysis presented in this paper are obtained follow the procedure proposed by Shadden et al. [22]. In this numerical analysis, the finite-time Lyapunov exponent (FTLE) is used to measure the repelling rate of the fluid in finite-time, and the attracting rate of the fluid can be measured by the backward time FTLE. For two-dimensional flow, FTLE can be expressed by the maximum eigenvalue of corresponding Cauchy-Green stress, which is

$$\sigma_{t_0}^T(\vec{x}) = \frac{1}{|T|} \ln \sqrt{\lambda_{\max} \left[\left(\frac{d\phi_{t_0}^{t_0+T}(\vec{x})}{d\vec{x}} \right)^* \left(\frac{d\phi_{t_0}^{t_0+T}(\vec{x})}{d\vec{x}} \right) \right]}, \quad (2.3)$$

where $\vec{x} = (x, y)$, $\sigma_{t_0}^T(\vec{x})$ is the FTLE in $[t_0, t_0+T]$, $\lambda_{\max}()$ is the maximum eigenvalue of a matrix, ϕ is the flow of system (2.1), $()^*$ is the transpose of a matrix. Then, the maximum attracting material lines, namely, attracting LCSs, can be revealed by the contour plot of the backward time FTLE field ($T < 0$). Accordingly, repelling LCSs can be revealed by the contour plot of the forward time FTLE field ($T > 0$). Although there are other definitions of LCSs and other numerical methods [23, 24], the FTLE field is still useful and easy to be computed. In the following, the FTLE field is used to reveal the LCSs, and several material lines are traced to verify the LCSs.

3 Governing equations and numerical methods

3.1 Numerical method for the flow around airfoil with LFS

For airfoil with LFS, ensuing self-induced oscillation, its boundary is moving, so ALE methods [25,26] and mesh moving technique [27] are used to study this problem numerically. The chord length of airfoil L is considered as characteristic scale, the free-stream velocity U is set as the characteristic velocity, and then dimensionless variables can be defined as

$$x^* = \frac{x}{L}, \quad y^* = \frac{y}{L}, \quad t^* = \frac{Ut}{L}, \quad p^* = \frac{p}{\rho_f U^2}, \quad u_i^* = \frac{u_i}{U}, \quad (3.1)$$

where ρ_f is the density of fluid, p and u_i are the pressure and velocity of the fluid, respectively. The Mach number of the flow studied is less than 0.3, so that the flow is considered as incompressible. For the sake of simplicity, (*) is dropped hereafter. Then, the governing equations for two-dimensional unsteady incompressible flow in the ALE configuration can be written as

$$\frac{\partial u_i}{\partial x_i} = 0, \quad (3.2a)$$

$$\frac{\partial u_i}{\partial t} + (u_j - \hat{u}_j) \frac{\partial u_i}{\partial x_j} = -\frac{\partial p}{\partial x_i} + \frac{1}{Re} \frac{\partial^2 u_i}{\partial x_j \partial x_j}, \quad (3.2b)$$

where \hat{u}_i is the velocity of the grid, Reynolds number $Re = \frac{\rho_f U L}{\mu}$, μ is the viscosity coefficient of fluid. The mesh moving strategy is implemented by spring analogy described in [26].

The characteristic based split (CBS) scheme [28] is introduced in ALE framework. Following the CBS scheme, the new coordinates along the characteristic line are applied to the system, then the convective terms can be removed, and the resulting equations become the simple diffusion equations in normal form, which can be solved efficiently by the standard finite element method. For clarify, the CBS procedures are summed up, and the detailed CBS scheme can be referred to Wang and Zhang [29]. Following the ALE-CBS methods, Eq. (3.2) can be solved as follows:

Step 1: Obtain the intermediate velocities u_i^* .

$$u_i^* - u_i^n = \Delta t \left(-c_j \frac{\partial}{\partial x_j} (u_i)^n + \frac{1}{Re} \frac{\partial^2 u_i^n}{\partial x_j \partial x_j} \right) + \frac{\Delta t^2}{2} c_k \frac{\partial}{\partial x_k} \left(\frac{\partial}{\partial x_j} (c_j u_i)^n + \frac{1}{Re} \frac{\partial^2 u_i^n}{\partial x_j \partial x_j} \right), \quad (3.3)$$

where $c_j = u_j - \hat{u}_j$.

Step 2: Solve the continuity equation.

$$\frac{\partial^2 p^{n+\theta}}{\partial x_i \partial x_i} = \theta \frac{\partial^2 p^{n+1}}{\partial x_i \partial x_i} + (1-\theta) \frac{\partial^2 p^n}{\partial x_i \partial x_i} = \frac{1}{\Delta t} \frac{\partial u_i^*}{\partial x_i}. \quad (3.4)$$

Step 3: Correct the velocities with obtained pressure.

$$u_i^{n+1} - u_i^* = -\Delta t \frac{\partial p^{n+\theta}}{\partial x_i}. \quad (3.5)$$

Eqs. (3.3), (3.4) and (3.5) are the temporal discretization forms of Navier-Stokes equations with CBS scheme, and can be approached easily by the standard finite element method. In this paper, the domain of flow is meshed by unstructured triangular elements, and the linear shape functions are used for the velocities and pressure in the spatial discretization, since the resulting governing equations are the diffusion equations in the common form.

3.2 Numerical methods for the flexible structure

For two-dimensional airfoil, the flexible structure on the surface can be modeled as a shallow arch [30,31], with simply supported boundary conditions. For such structure, its self-excited oscillation can be induced by the unsteady aerodynamic forces. As shown in Fig. 2, the shallow arch has a rectangular cross section with thickness h and chord length l .

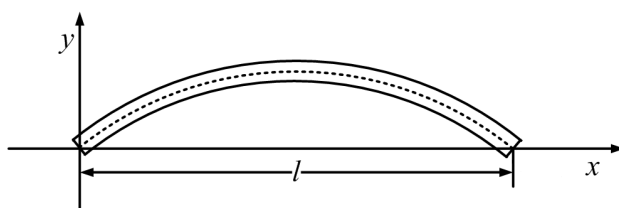


Figure 2: Schematics of the shallow arch.

The governing equation of shallow arch is

$$\rho_s h \frac{\partial^2 w}{\partial t^2} + d \frac{\partial w}{\partial t} + \frac{Eh^3}{12} w'''' + V(y_0'' - w'') = f, \quad (3.6)$$

where $()'$ is partial differential of x , ρ_s is the density of arch, h is the thickness, d is the damped coefficient of the system, E is the modulus of elasticity, $V = \frac{1}{l} \int_0^l \frac{Eh}{2} (y^2 - y_0^2) dx$, y_0 is the initial position of arch, w is the position of arch during oscillation, $w = y - y_0$. The aerodynamic force f is the pressure difference on both side of arch, $f = \Delta p$, since the viscous stresses are small and neglectable compared with the pressure difference. In order to couple with the fluid flow, the parameters in Eq. (3.6) are dimensionless and defined as

$$l^* = \frac{l}{L}, \quad h^* = \frac{h}{L}, \quad w^* = \frac{w}{L}, \quad \rho_s^* = \frac{\rho_s}{\rho_f}, \quad E^* = \frac{E}{\rho_f U^2}, \quad f^* = \frac{f}{\rho_f U^2}, \quad (3.7)$$

where ρ_f is the density of fluid, the (*) is dropped in Eq. (3.6) for the sake of simplicity.

The simply supported boundary conditions and initial conditions are given as

$$w|_{x=0} = w|_{x=l} = 0, \tag{3.8}$$

$$t=0: \quad w=0, \quad \frac{\partial w}{\partial t} = 0. \tag{3.9}$$

The initial shape or configuration of the arch is approached by second-order polynomial. With the boundary conditions (3.8), the initial shape of the shallow arch has the form

$$y_0(x) = -blx + bx^2. \tag{3.10}$$

Galerkin procedure is used to approach Eq. (3.6). The linear operator in Eq. (3.6) with boundary condition (3.8) has a complete set of eigenfunctions $\{\sin \frac{n\pi}{l}x, n = 1, 2, \dots, n\}$, which spans an orthogonal basis of the space onto which the solution of the governing equation can be projected [31]. So the solution of Eq. (3.6) can be written in the following form,

$$w(x,t) = \sum_{n=1}^{\infty} w_n(t) \sin \frac{n\pi}{l}x. \tag{3.11}$$

Following the Galerkin procedure, the general form of Eq. (3.6) can be obtained as

$$\begin{aligned} & \frac{Eh^3}{12}w_m \frac{(m\pi)^4}{2l^3} + \sum_{n=1}^{\infty} \left\{ w_n^2 \frac{(n\pi)^2}{2l} \frac{Eh}{2l} + \frac{2Ebh}{n\pi}w_n[(-1)^{n+1} + 1] \right\} 2b \frac{l}{m\pi} [(-1)^{m+1} + 1] \\ & + \sum_{n=1}^{\infty} \left\{ w_n^2 \frac{(n\pi)^2}{2l} \frac{Eh}{2l} + \frac{2Ebh}{n\pi}w_n[(-1)^{n+1} + 1] \right\} w_m \frac{(m\pi)^2}{2l} \\ & + \frac{\rho hl}{2}\ddot{w}_m + \frac{ld}{2}\dot{w}_m - \int_0^l f \sin \left(\frac{m\pi}{l}x \right) dx = 0 \quad (m = 1, 2, \dots, +\infty). \end{aligned} \tag{3.12}$$

Eq. (3.12) is solved by the fourth-order Runge-Kutta algorithm coupling with the aerodynamic solver, and dynamic behaviors of the flexible surface can be obtained.

In this paper, the first 10 modes are considered, and the coupling between fluid and structure is implemented using loosely coupling strategy with time step less than 10^{-4} .

3.3 Verifications of the numerical scheme for fluid-structure interaction

To verify the fluid-structure interaction model and numerical method presented, several cases of flow around a membrane with $Re = 2500$ are simulated numerically and compared with the existing results, which are related to micro air vehicle and presented by Gordnier [1]. As shown in Fig. 3(a), the membrane consists of a thin sheet stretched between two small, aerodynamically shaped, rigid mounts (lower figure in Fig. 3(a)). The non-dimensional parameters of membrane are $\rho_s h = 0.589$ and $Eh = 50$.

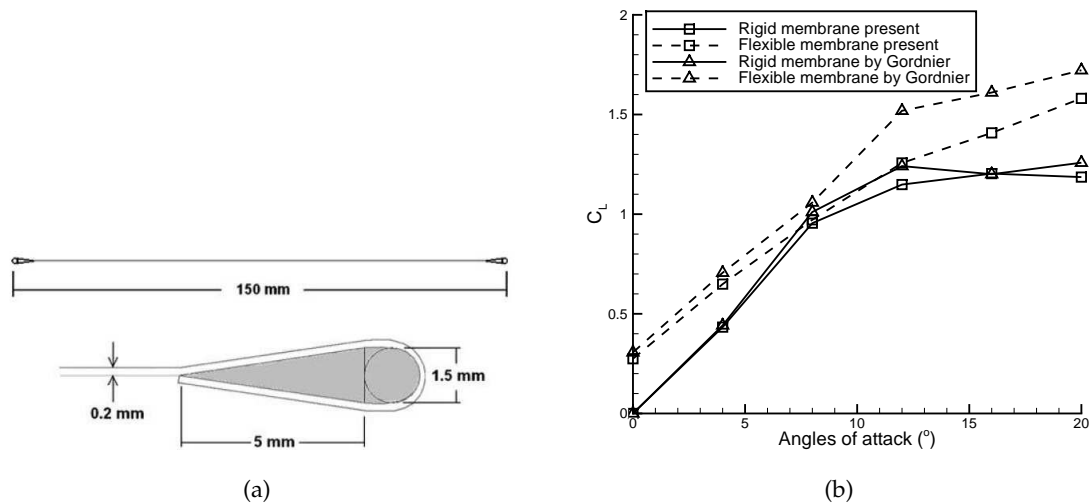


Figure 3: Model of membrane [1] (a) and variation of lift coefficient vs. angle of attack (b).

The results from present algorithm are in agreement with the results given by Gordnier [1] for rigid flat airfoil, as shown in Fig. 3(b). For flexible membrane, the lift coefficients at low angles of attack (AOA) agree well with Gordnier's work. As the AOA is increasing, there exists a difference between present results and Gordnier's results. This is caused by the bending effect (third terms on left side of Eq. (3.6)) considered in shallow arch model in this study. Compared with the membrane model used by Gordnier, the bending effect can cause the reduction of the deformation of the arch under the same aerodynamic load. Smaller deformation means weaker camber effect and smaller lift coefficient. At high AOA, the deformation of structure is large, and the reduction of deformation caused by the bending effect is great. Hence, there exists large discrepancy between present results and Gordnier's results at high AOA. Even at low AOA, the lift coefficients for flexible membrane of present results are still smaller than the lift coefficients obtained by Gordnier, due to the bending effect.

4 Numerical results and analysis

In this study, NACA0012 airfoil with LFS is chosen as an example. In particular, the Reynolds number is set as 5000 for all cases. The local flexible skin is located at 0–0.1 chord length of airfoil, as shown in Fig. 4, from where the perturbation can be easily transported into the separated area. Because this study mainly focuses on the unsteady flow separation and flow structures induced by the oscillation of LFS, the dimensionless parameters of shallow arch keep fixed with a constant mass ratio $\rho_s h = 5.85$, thickness $h = 0.001$, structural damped coefficient $d = 0.5$. The Young's modulus of the structure is chosen as $Eh = 80$, which is the same order of magnitude as used in [1].

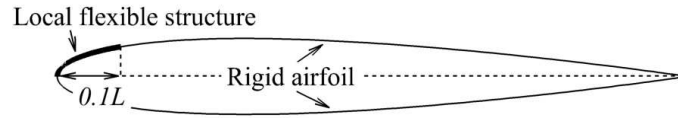


Figure 4: Schematics of airfoil with LFS.

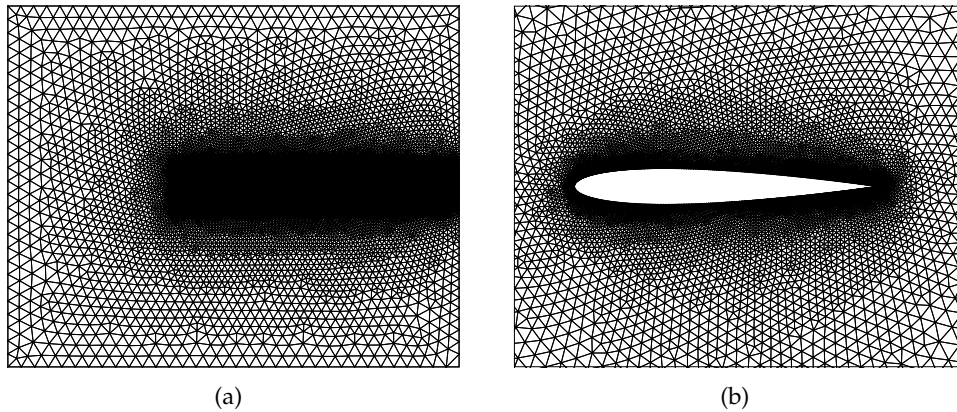


Figure 5: Grid of computational domain (a) and detailed grid near the airfoil(b).

The computational domain is a rectangle region of $[-10,15] \times [-10,-10]$, and meshed by unstructured triangular elements. To verify the independent of the mesh quality, three type of meshes are used to study the case with AOA $\alpha = 6^\circ$ and $Re = 5000$, and the results are listed in Table 1. By comparison, it is clear that Mesh2 as shown in Fig. 5 is robust.

Table 1: Lift and drag coefficients obtained by different meshes for rigid airfoil at $\alpha = 6^\circ$.

Mesh No.	Number of nodes	Lift coefficient	Drag coefficient
Mesh1	13161	0.28821	0.0775
Mesh2	19720	0.28916	0.07818
Mesh3	28746	0.28965	0.07823

4.1 Self-induced oscillation of the LFS

Under the periodic aerodynamic force, the LFS oscillates periodically, that is, the oscillation is self-induced and periodical. The amplitudes of first four modes at $\alpha = 6^\circ$ are presented in Fig. 6(a), where w_n is the amplitude of n th mode involved in the response. It shows that the amplitude of each mode oscillates periodically, and the first mode plays a significant role in the response. The oscillation amplitudes of first four modes at different angles of attack are shown in Fig. 6(b). It can be seen that the amplitude of each mode is very small at lower AOA and increases significantly beyond $\alpha = 5^\circ$. As AOA is increasing

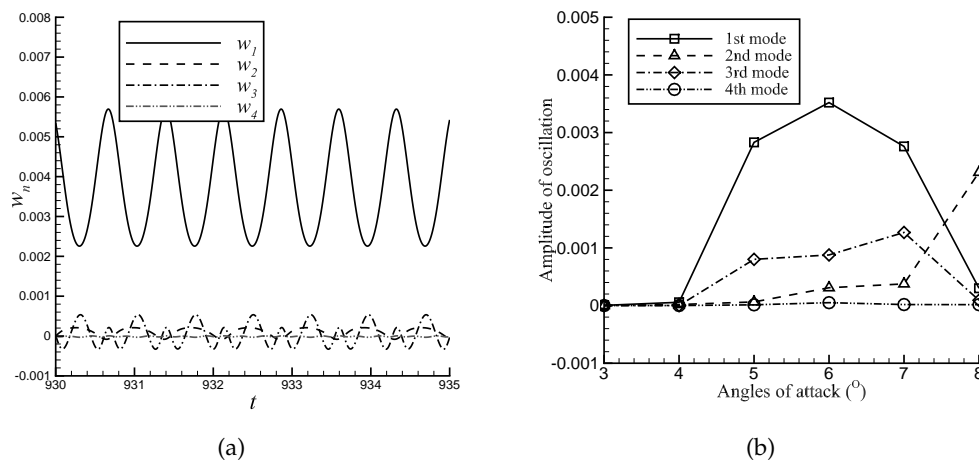


Figure 6: The oscillation of the arch. (a) The time history of amplitudes of first four modes at $\alpha = 6^\circ$. (b) The oscillation amplitudes of first four modes at different angles of attack.

further, the amplitude keeps in order of magnitude ($o(10^{-3})$), implying a small amount of energy exchange between fluid and structure. However, such small amplitude of oscillation is essential to lift enhancement, since it can induce the fluctuation of velocity, and eventually change the flow structure. Such influence will be studied further by LCSs in following sections.

4.2 Influences of the LFS on lift enhancement

The time-averaged lift and drag coefficients of the airfoil with LFS at various angles of attack are compared with rigid one, as shown in Fig. 7.

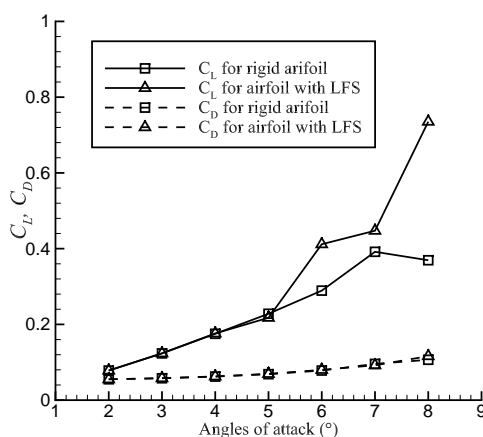


Figure 7: Lift and drag coefficients of different airfoils at various angles of attack.

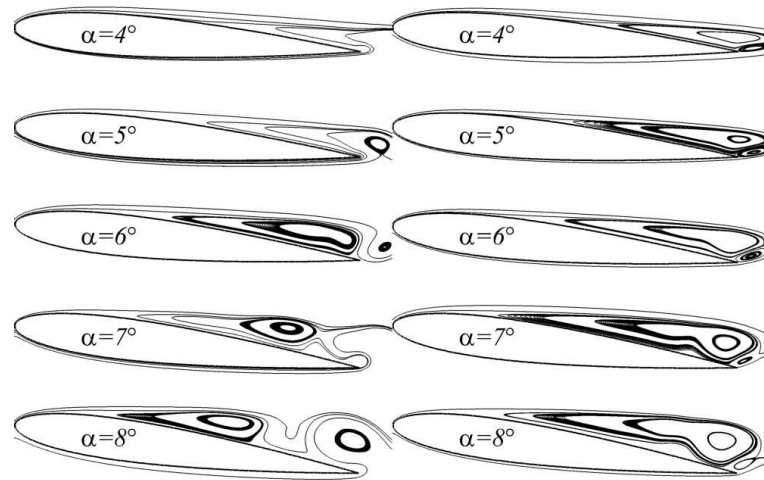


Figure 8: Instantaneous streamlines (left column) and time-averaged streamlines (right column) of rigid airfoil.

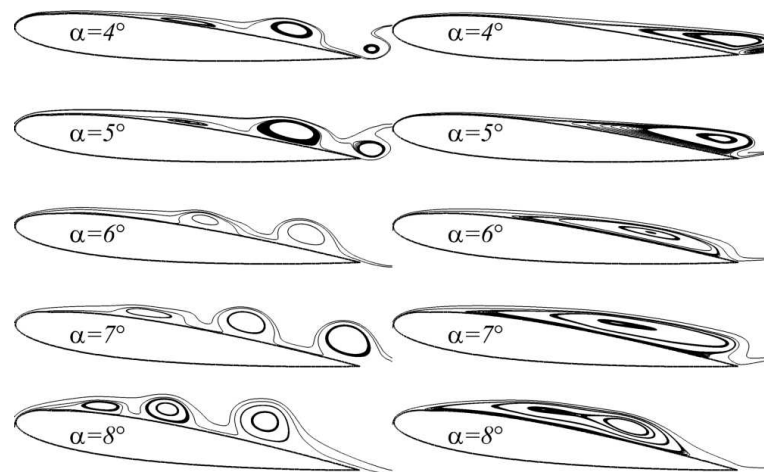


Figure 9: Instantaneous streamlines (left column) and time-averaged streamlines (right column) of airfoil with LFS.

At small AOA, the flexible structure has a slight influence on the lift and drag coefficients. As AOA increases beyond 5° , the lift coefficient of airfoil with LFS is increased rapidly than rigid one, while its drag coefficient is almost same as rigid one. It is clear that the rapid changing of lift is consistent with the sudden jump of the oscillation amplitude of arch shown in Fig. 6(b), except for case with $\alpha = 5^\circ$.

From the instantaneous streamlines shown in left column of Fig. 8, it can be seen that the streamline patterns of rigid airfoil at different angles of attack are similar with the flow over normal bluff body. In the time-averaged streamlines shown in right column of

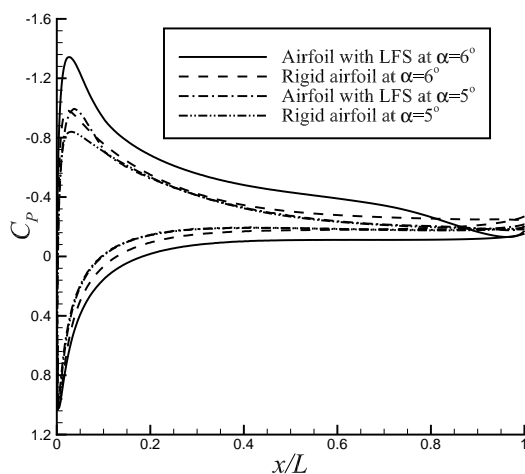


Figure 10: Comparisons of time-averaged pressure coefficients between rigid airfoil and airfoil with LFS at $\alpha=5^\circ$ and $\alpha=6^\circ$.

Fig. 8, there is large separation bubble attached on the airfoil at each AOA. The separated area increases and separation point moves upstream as the AOA increasing.

For flow over airfoil with LFS, as shown in Fig. 9, the instantaneous streamlines and time-averaged streamlines are similar to the one of rigid airfoil at low angles of attack, since the oscillation amplitude of LFS is small. At $\alpha=5^\circ$, an individual separation bubble appears on the airfoil with LFS, and the oscillation amplitude of LFS increases greatly. As the AOA is increasing further, more individual separation bubbles emerge on the airfoil, and their birth locations are closer to the leading edge. From time-averaged streamlines, the reduction of separated area is consistent with the lift enhancement of airfoil. At $\alpha=6^\circ \sim 8^\circ$, the separated area is reduced significantly, and the lift of airfoil increases in large degree. Additionally, the time-averaged pressure coefficients on airfoil surface at $\alpha=6^\circ$ (shown in Fig. 10) also shows that the time-averaged pressure on the upper surface of airfoil with LFS is much lower than that of rigid airfoil. However, At $\alpha=5^\circ$, the individual separation bubbles, similar with that of airfoil at $\alpha=6^\circ$, fail to reduce the separation area and enhance the lift. The time-averaged pressures on the upper surface of airfoil with LFS at $\alpha=5^\circ$ are the same as that of rigid airfoil, as shown in Fig. 10.

In general, the individual separation bubble and its evolution on the upper surface of airfoil are the key factors for the lift enhancement. Therefore, the flow structures, dominated by individual separation bubbles, of airfoil with LFS at $\alpha=6^\circ$ are studied in detail from Lagrangian viewpoints and compared to the one of rigid airfoil.

4.3 Flow structures under unsteady flow separation

In this section, the LCSs are used to study the flow structures from Lagrangian viewpoint. The LCSs can capture the material spikes and reveal the transport and mixing in the flow.

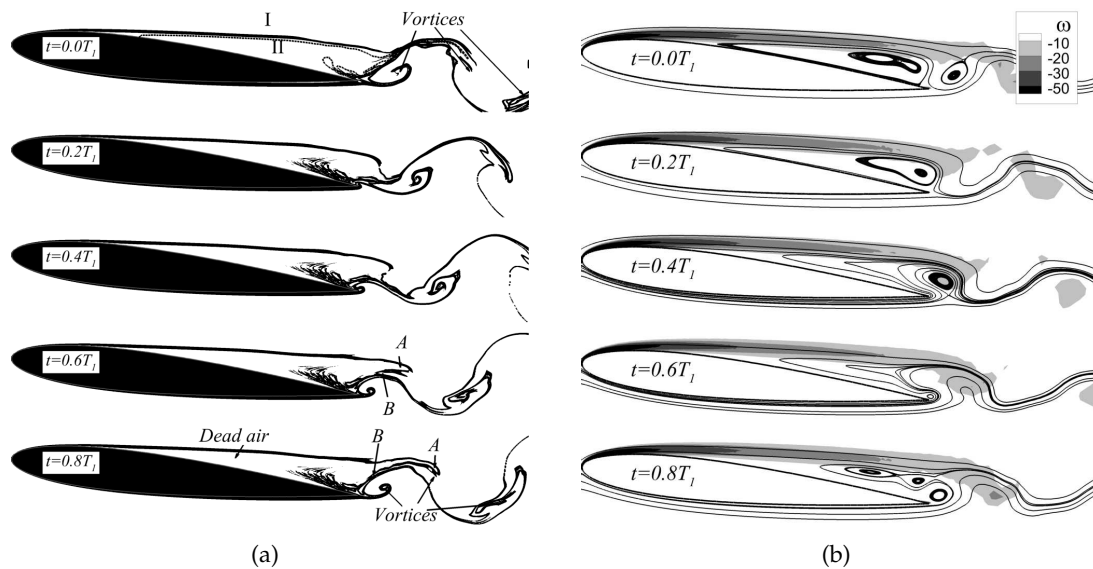


Figure 11: Attracting LCSs (a) and streamline structures (b) in one period of flow over rigid airfoil at $\alpha = 6^\circ$.

Hence, one can understand the nature of unsteady separation by studying the transport and mixing in the flow. For the periodic flow, there is a fixed separation point on the boundary, according to the fixed separation criteria [13] (see Eqs. (2.2)). Then, the unstable manifold of the fixed separation point can be approached by tracing a short material line connected to the fixed separation point.

Two cases are studied in this section, rigid airfoil and airfoil with LFS at $\alpha = 6^\circ$. Note that the periods are different for two cases, and hereafter T_1 denotes the period for rigid airfoil, T_2 for airfoil with LFS.

In one period, the attracting LCSs and the corresponding streamline structures for rigid airfoil are shown in Fig. 11. Among them, the LCSs are revealed by the contour plots of backward time FTLE field, and the dashed lines are the unstable manifold of fixed separation point for verification of LCSs.

For the flow around rigid airfoil, the unstable manifold of the fixed separation point (dashed line in Fig. 11(a)) splits the upper flow into two parts, main flow *I* and separated flow *II*, as shown in Fig. 11(a). Near the separation point, the attracting LCSs are nearly steady until reach the rear of airfoil where the attracting LCSs are stretched intensely. As shown in Fig. 11, some fluid particles (e.g. *A* in Fig. 11(a)) in region *II* are transported into main flow *I*, and some fluid particles (e.g. *B* in Fig. 11(a)) in region *I* are transported into main flow *II*. It's clear that in the separated flow *II*, transport and mixing are only restricted in the region near the rear of airfoil, leaving rest of the separated flow, called dead air region, untouched. The vortices are generated behind the region *II*, as shown in the vorticity contour, along with the transport of fluid from separated flow to the wake. Pressure distributions on the surface of airfoil in one period, as shown in Fig. 12, show

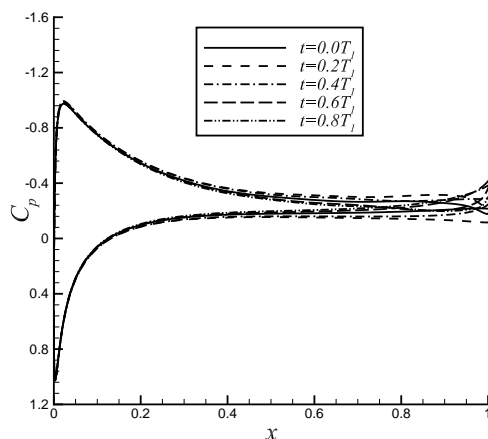


Figure 12: Pressure coefficients in one period of rigid airfoil at $\alpha=6^\circ$.

that the transports in the wake have little influences on the pressure distribution of airfoil.

For flow over airfoil with LFS at $\alpha=6^\circ$, the LCSs are quite different from that of rigid one, as shown in Fig. 13. Near the leading edge of airfoil, the LCSs (U_0 in Fig. 13(a)) hover over the boundary, which are caused by the no-slip boundary conditions and the shear layer near the boundary. This part of LCSs are called shear LCSs or weak LCSs according to Haller [24]. There are several material spikes, attracting LCSs U_1 , U_2 and U_3 , lying on the upper surface of airfoil. In the Poincaré map, they are the same material spike

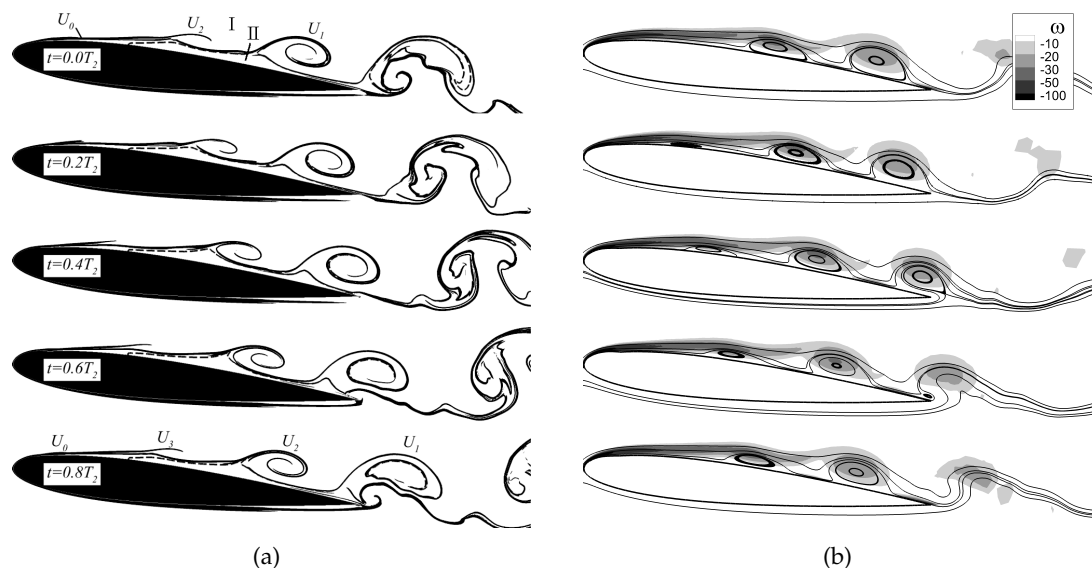


Figure 13: Attracting LCSs (a) and streamline structures (b) in one period of flow over airfoil with LFS at $\alpha=6^\circ$. (Dashed line is the unstable manifold of the fixed separation point.)

on different Poincaré sections. In each period, the flexible structure moves up and down, and the flow particles passing by will gain and lose kinetic energy. Consequently, the flow particles along the airfoil surface have non-uniform velocity in both x and y direction, and result in the generation of separation bubble and material spike from shear layer. Then, the material spike (U_3 in Fig. 13(a)) rotates inward to form a vortex as it moves downstream. Follow the material spike, large amount of flow particles in main flow will be transported into the vortex.

The unstable manifold of the fixed separation point in airfoil with LFS (dashed lines in Fig. 13(a)) also splits the flow into two parts: main flow I and separated flow II , as that of rigid airfoil. However, the separated flow is suppressed obviously by the oscillation of LFS. The vortices generated by the moving material spikes are the main factors, since they can transport the flow particles with high kinetic energy from main flow to the boundary layer.

As a new material spike, U_2 for example, appears, the unstable manifold of fixed separation point fails to capture it until the spike moves to the downstream. This indicates that the material spike is not induced by the unstable manifold of fixed separation, and the unsteady separation relevant to the generation of vortex should be another type of separation, rather than the fixed separation.

In order to study the new type of unsteady flow separation of airfoil with LFS at $\alpha = 6^\circ$ in detail, both the attracting (gray solid lines) and repelling (gray dashed lines) LCSs are computed and shown in Fig. 14. It can be seen that there are several saddle type

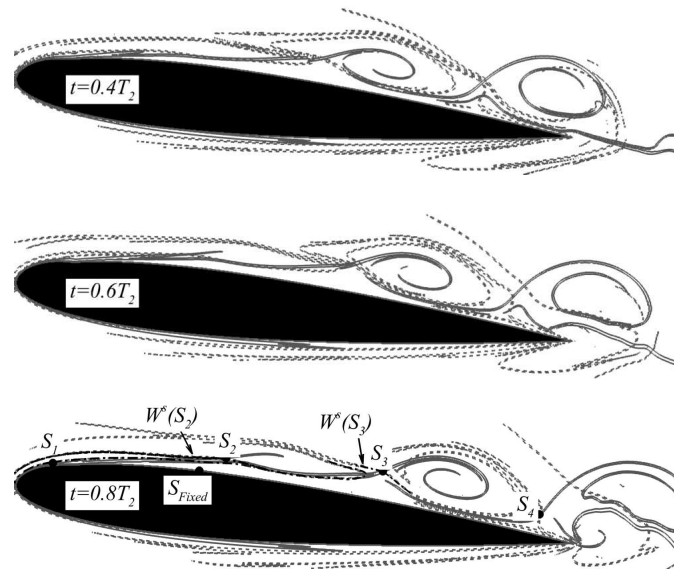


Figure 14: Attracting and repelling LCSs at $\alpha = 6^\circ$. (Gray solid lines denote attracting LCSs, gray dashed lines denote repelling LCSs, black dashdot lines are material lines.)

points S_2 - S_4 at which the attracting and repelling LCSs intersect each other. By tracing the material line $W^s(S_3)$ (black dashdot lines) connected to S_3 , it can be seen that the saddle type points and their stable manifolds satisfy $S_1 = P^{-2}(S_3)$, $S_2 = P^{-1}(S_3)$, $S_4 = P(S_3)$, $W^s(S_2) = P^{-1}(W^s(S_3))$, where $P: X(t) \mapsto X(t+T_2)$ is the Poincaré map associated with period T_2 of the flow. The point S_1 indicates that the saddle type points S_2 - S_4 come from the shear layer at the leading edge of airfoil, instead of the flow near fixed separation point. Such separation can be considered as moving separation according the definition proposed by Surana and Haller [14], since the material spike and the associated saddle point (S_2 - S_4) move downstream along the airfoil surface. Near the leading edge of airfoil, the repelling LCSs divide the boundary layer into several layers. Particles in each layer are transported from main flow into a vortex along the material spikes. Eventually, the vortices are formed by a large amount of flow particles transported from main flow, and the high kinetic energies they carried can be injected into the dead air near the no-slip boundary, suppressing the separation and reducing the separated region *II*. In region *II*, flow particles are trapped by the moving separation. This phenomenon is similar to the flow over rotating circular cylinder, in which fluid close to the cylinder can never separate from boundary.

In general, the lift of the airfoil depends strongly on the dead air region in the separated flow, e.g. the area of region *II* for both rigid airfoil and airfoil with LFS. The moving separation can induce vortex with low pressure above the separated region, and reduce the separated region by removing the dead air.

Even though the moving separation can induce vortex with low pressure, the pressure distribution between two vortices is still high. As shown in Fig. 13 and Fig. 14, between two vortices, there is large area that belongs to region *II*, and its scale increases as vortex growing big. From the pressure distributions on the airfoil as shown in Fig. 15(b), pressure on upper surface of airfoil fluctuates violently. Pressure near the moving vortices maintains a low value, yet the pressure between the vortices keep increasing as the vortices move to the trailing edge of airfoil. From the time-averaged pressure distribution of airfoil with LFS at $\alpha = 6^\circ$ shown in Fig. 10, the moving vortices have no contribution to the lift enhancement at the trailing edge of airfoil. At the leading edge, the pressure oscillation caused by the LFS changes the pressure gradient along the airfoil surface, which also is the key factor to the generation and movement of individual separation bubble.

For airfoil with LFS at $\alpha = 5^\circ$, the flow structures and the unsteady flow separation are similar with the one of airfoil with LFS at $\alpha = 6^\circ$, nevertheless, there is no lift enhancement obtained. From the pressure distribution shown in Fig. 15(a), the pressure at the leading edge is higher and the adverse pressure gradient is weaker than that of airfoil with LFS at $\alpha = 6^\circ$. Eventually, the downstream moving separation bubbles and vortices with concentration of vorticity appear close to the trailing edge of airfoil. Before the vortex grows strong enough to reduce the pressure, it starts to shed from the airfoil. For airfoil with LFS at $\alpha = 7^\circ$ and $\alpha = 8^\circ$, as shown in Figs. 15(c) and 15(d), the vortex generates close to the leading edge and can stay on the airfoil for long time, and the corresponding lift enhancement are significant.

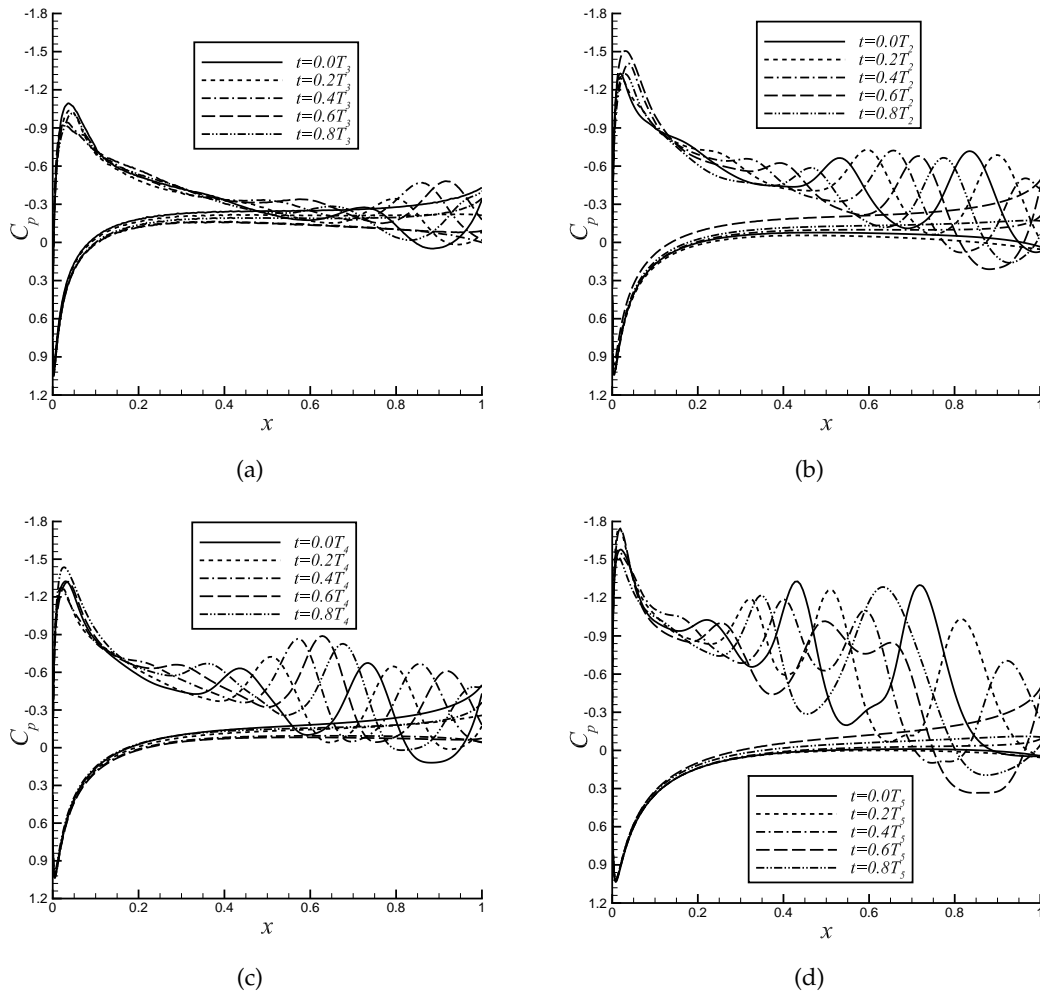


Figure 15: Pressure coefficients in one period of airfoil with LFS. (a) $\alpha = 5^\circ$, (b) $\alpha = 6^\circ$, (c) $\alpha = 7^\circ$, (d) $\alpha = 8^\circ$.

5 Conclusions

The flow structures of unsteady flow separation over airfoil with LFS are studied numerically from viewpoint of Lagrangian frames in detail, in order to investigate the nature of its high aerodynamic performance. The phenomenon with downstream moving vortices on the upper surface of airfoil, induced by the oscillation of the LFS, is considered as main reason for the lift enhancement. The evolution of attracting and repelling LCSs shows that the transport between shear layer and main flow is enhanced by the LFS. Meanwhile, the small scale vortices induced by the moving material spikes, proved to be moving separation, can transport the kinetic energy from main flow into the separated flow. Consequently, the separated area and dead air region are reduced significantly, re-

sulting in the pressure reduction on the upper surface of airfoil. Further, the study shows the flow separation can be controlled feasibly using the LFS on the surface of the airfoil, inducing unsteadiness and transport, and there exists a rich variety of dynamics which can be used to enhance the lift.

Acknowledgments

This work was supported by the National Fundamental Research Program of China (973 Program), No. 2012CB026002, and the National High Technology Research Program of China (863 Program), No. 2012AA052303.

References

- [1] R. E. Gordnier, High fidelity computational simulation of a membrane wing airfoil, *Journal of Fluids and Structures*, 25(2009), 897-917.
- [2] P. Rojratsirikul, Z. Wang, and I. Gursul, Unsteady aerodynamics of membrane wing airfoil, *AIAA Paper*, 2008-0613.
- [3] U. K. Chakravarty and R. Albertani, Experimental and finite element modal analysis of a pliant elastic membrane for micro air vehicles applications, *Journal of Applied Mechanics*, 79(2012), 021004.
- [4] D. W. Zingg, L. Diosady, and L. Billing, Adaptive airfoils for drag reduction at transonic speeds, *AIAA Paper*, 2006-3656.
- [5] N. J. Pern and J. D. Jacob, Wake vortex mitigation using adaptive airfoils - The Piezoelectric Arc Airfoil, *AIAA Paper*, 1999-0524.
- [6] S. K. Chimakurthi, J. Tang, R. Palacios, C. E. S. Cesnik, and W. Shyy, Computational aeroelasticity framework for analyzing flapping wing micro air vehicles, *AIAA Journal*, 47(2009), 1865-1878.
- [7] K. B. Lee, J. H. Kim, and C. Kim, Aerodynamic effects of structural flexibility in two-dimensional insect flapping flight, *Journal of Aircraft*, 48(2011), 894-909.
- [8] W. Kang, J. Z. Zhang, and P. H. Feng, Aerodynamic analysis of a localized flexible airfoil at low Reynolds numbers, *Communications in Computational Physics*, 11(2012), 1300-1310.
- [9] W. R. Sears, and D. P. Telionis, Boundary-layer separation in unsteady flow, *SIAM Journal on Applied Mathematics*, 28(1975), 215-235.
- [10] L. L. Van Dommelen and S. J. Cowley, On the Lagrangian description of unsteady boundary layer separation, part 1. General Theory, *Journal of Fluid Mechanics*, 210(1990), 593-626.
- [11] J. Duan and S. Wiggins, Lagrangian transport and chaos in the near wake of the flow around an obstacle: a numerical implementation of lobe dynamics, *Nonlinear Processes in Geophysics*, 4(1997), 125-136.
- [12] G. Haller and G. Yuan, Lagrangian coherent structures and mixing in two-dimensional turbulence, *Physica D*, 147(2000), 352-370.
- [13] G. Haller, Exact theory of unsteady separation for two-dimensional flows, *Journal of Fluid Mechanics*, 512(2005), 257-311.
- [14] A. Surana and G. Haller, Ghost manifolds in slow-fast systems, with applications to unsteady fluid flow separation, *Physica D: Nonlinear Phenomena*, 237(2008), 1507-1529.

- [15] D. Lipinski, B. Cardwell, and K. Mohseni, A Lagrangian analysis of a two-dimensional air-foil with vortex shedding, *Journal of Physics A: Mathematical and Theoretical*, 41(2008), 344011.
- [16] F. J. Beron-Vera, M. J. Olascoaga, and G. J. Goni, Oceanic mesoscale eddies as revealed by Lagrangian coherent structures, *Geophysical Research Letters*, 35(2008), L12603.
- [17] A. E. BozorgMagham, S. D. Ross, and D. G. Schmale, Real-time prediction of atmospheric Lagrangian coherent structures based on forecast data: an application and error analysis, *Physica D: Nonlinear Phenomena*, 258(2013), 47-60.
- [18] M. Mathur, G. Haller, T. Peacock, J. Ruppert-Felsot, and H. Swinney, Uncovering the Lagrangian skeleton of turbulence, *Physical Review Letters*, 98(2007), 144502.
- [19] M. A. Green, C. W. Rowley, and G. Haller, Detection of Lagrangian coherent structures in three-dimensional turbulence, *Journal of Fluid Mechanics*, 572(2007), 111-120.
- [20] M. Weldon, T. Peacock, G. B. Jacobs, M. Helu, and G. Haller, Experimental and numerical investigation of the kinematic theory of unsteady separation, *Journal of Fluid Mechanics*, 611(2008), 1-11.
- [21] G. Haller, Finding finite-time invariant manifolds in two-dimensional velocity fields, *Chaos*, 10(2000), 99-108.
- [22] S. C. Shadden, F. Lekien, and J. E. Marsden, Definition and properties of Lagrangian coherent structures from finite-time Lyapunov exponents in two-dimensional aperiodic flows, *Physica D: Nonlinear Phenomena*, 212(2005), 271-304.
- [23] D. Lipinski and K. Mohseni, A ridge tracking algorithm and error estimate for efficient computation of Lagrangian coherent structures, *Chaos: An Interdisciplinary Journal of Nonlinear Science*, 20(2010), 017504.
- [24] G. Haller, A variational theory of hyperbolic Lagrangian coherent structures, *Physica D: Nonlinear Phenomena*, 240(2011), 574-598.
- [25] P. Kjellgren and J. Hyvarinen, An arbitrary Lagrangian-Eulerian finite element method, *Computational Mechanics*, 21(1998), 81-90.
- [26] J. Sarrate, A. Huerta, and J. Donea, Arbitrary Lagrangian-Eulerian formulation for fluid-rigid body interaction, *Computer Methods in Applied Mechanics and Engineering*, 190(2001), 3171-3188.
- [27] J. T. Batina, Unsteady Euler airfoil solutions using unstructured dynamic mesh, *AIAA Journal*, 28(1990), 1381-1388.
- [28] P. Nithiarasu, A fully explicit characteristic based split (CBS) scheme for viscoelastic flow calculations, *International Journal for Numerical Methods in Engineering*, 60(2004), 949-978.
- [29] Y. T. Wang and J. Z. Zhang, An improved ALE and CBS-based finite element algorithm for analyzing flows around forced oscillating bodies, *Finite Elements in Analysis and Design*, 47(2011), 1058-1065.
- [30] J. Z. Zhang and D. H. van Campen, Stability and bifurcation of doubly curved shallow panels under quasi-static uniform load, *International Journal of Non-linear Mechanics*, 38(2003), 457-466.
- [31] J. Z. Zhang, Y. Liu, P. F. Lei, and X. Sun, Dynamic snap-through buckling analysis of shallow arches under impact load based on approximate inertial manifolds, *Dynamics of Continuous Discrete and Impulsive Systems-Series B-Applications and Algorithms*, 14(2007), 287-291.